frontiers in Chemistry

ORIGINAL RESEARCH
published: 28 August 2018
doi: 10.3389/fchem.2018.00389

Size-Tunable Natural Mineral-Molybdenite for Lithium-Ion Batteries Toward: Enhanced Storage Capacity and Quicken Ions Transferring

Feng Jiang[1], Sijie Li[2,3], Peng Ge[2,3], Honghu Tang[2], Sultan A. Khoso[1], Chenyang Zhang[1], Yue Yang[1], Hongshuai Hou[2,3], Yuehua Hu[1], Wei Sun[1] and Xiaobo Ji[2,3]**

[1] School of Minerals Processing and Bioengineering, Central South University, Changsha, China, [2] College of Chemistry and Chemical Engineering, Central South University, Changsha, China, [3] State Key Laboratory of Powder Metallurgy, Central South University, Changsha, China

OPEN ACCESS

Edited by:
Qiaobao Zhang,
Xiamen University, China

Reviewed by:
Huixin Chen,
Xiamen Institute of Rare Earth Materials, China
Yunhua Xu,
Tianjin University, China
Xianwen Wu,
Jishou University, China

***Correspondence:**
Wei Sun
sunmenghu@csu.edu.cn
Xiaobo Ji
xji@csu.edu.cn

Specialty section:
This article was submitted to Physical Chemistry and Chemical Physics, a section of the journal Frontiers in Chemistry

Received: 06 July 2018
Accepted: 13 August 2018
Published: 28 August 2018

Citation:
Jiang F, Li S, Ge P, Tang H, Khoso SA, Zhang C, Yang Y, Hou H, Hu Y, Sun W and Ji X (2018) Size-Tunable Natural Mineral-Molybdenite for Lithium-Ion Batteries Toward: Enhanced Storage Capacity and Quicken Ions Transferring. Front. Chem. 6:389. doi: 10.3389/fchem.2018.00389

Restricted by the dissatisfied capacity of traditional materials, lithium-ion batteries (LIBs) still suffer from the low energy-density. The pursuing of natural electrode resources with high lithium-storage capability has triggered a plenty of activities. Through the hydro-refining process of raw molybdenite ore, containing crushing–grinding, flotation, exfoliation, and gradient centrifugation, 2D molybdenum disulfide (MoS_2) with high purity is massively obtained. The effective tailoring process further induce various sizes (5, 2, 1 and 90 nm) of sheets, accompanying with the increasing of active sites and defects. Utilized as LIB anodes, size-tuning could serve crucial roles on the electrochemical properties. Among them, MoS_2-1 μm delivers an initial charge capacity of 904 mAh g^{-1}, reaching up to 1,337 mAh g^{-1} over 125 loops at 0.1 A g^{-1}. Even at 5.0 A g^{-1}, a considerable capacity of 682 mAh g^{-1} is remained. Detailedly analyzing kinetic origins reveals that size-controlling would bring about lowered charge transfer resistance and quicken ions diffusion. The work is anticipated to shed light on the effect of different MoS_2 sheet sizes on Li-capacity ability and provides a promising strategy for the commercial-scale production of natural mineral as high-capacity anodes.

Keywords: natural molybdenite ore, molybdenum disulfide, size effect, lithium-ion battery, electrochemical performance

INTRODUCTION

Lithium-ion batteries (LIBs) are renewable energy storage devices commonly used in consumer electronics, high-power tools, and electric vehicles because of their excellent capacities, such as high energy density, long cycle life, low self-discharge, no memory effect (Li et al., 2017; Yang et al., 2017; Zhang et al., 2018; Zheng et al., 2018). Graphite is the current commercial anode material due to its flat potential profile and great structure stability during cycling. However, six carbon atoms are required to accommodate one Li ion, and the theoretical specific capacity (372 mAh g^{-1}) of graphite is insufficient to meet the increasing requirements of the ever-growing market of high-performance batteries(Shim and Striebel, 2003; Yoshio et al., 2003, 2004).

Two-dimensional (2D) metal dichalcogenides (MDCs) as an alternative material for graphite has received considerable attention(Chhowalla et al., 2013; Yang et al., 2015; Zhang et al., 2015; Ge et al., 2018a,b). Among them, molybdenum disulfide is a typical graphene analog, in which two adjacent S-Mo-S layers are linked by weak van der Waals forces. Given its novel mechanical, optical, electrical, and electrochemical properties, MoS_2 has been widely studied for different applications in lubricants(Xiao et al., 2017; Wu et al., 2018), photocatalytic degradation catalysts(Li et al., 2014; Su et al., 2016; Liu et al., 2018), sensors(Liu et al., 2014; Wang and Ni, 2014), electrocatalytic hydrogen generation(Gao et al., 2015a,b; Zhu et al., 2015; Geng et al., 2016), field-effect transistors(Dankert et al., 2014; Roy et al., 2014), supercapacitors(Ma et al., 2013; Acerce et al., 2015), and electrode material for batteries(Liang et al., 2011; Yang et al., 2015; Hai et al., 2018). Compared with graphite, MoS_2 has a wider lattice spacing (∼0.65 nm), which is conducive to rapid insertion and extraction of alkali metal ions. After insertion, Li_xMoS_2 can further react with Li^+ ions to form Li_2S and Mo atom, and the theoretical specific capacity of MoS_2 in LIBs is 670 mAh g^{-1}, which is much higher than that of graphite (Stephenson et al., 2014). Meanwhile, a number of studies reported that the capacity of MoS_2 can reach >1,000 mAh g^{-1}, which arises from Mo atoms accommodating a large amount of Li ions over prolonged discharging process (Wang et al., 2018).

Most previous studies synthesized MoS_2 by chemical methods to obtain nanosheets with desired size and thickness. Hydrothermal, chemical vapor deposition, and hot injection are typical approaches that use molybdenum salts as precursors (Altavilla et al., 2011; Wang et al., 2014). Although the aforementioned chemical synthetic methods can be used for the large-scale preparation of MoS_2 nanosheets, their industrial applications are limited by their rigid reaction conditions and environmentally pernicious reactants (Yang et al., 2016, 2018; Zhang et al., 2016). MoS_2 is abundant in the form of molybdenite in nature and is generally extracted and processed into molybdenum metal and compounds through beneficiation, smelting and chemical synthesis. Thus, fabrication of MoS_2 materials directly from natural molybdenite ore can eliminate many intermedia complex processes and reduce synthetic contaminants. In addition, the appropriate size of MoS_2 for LIBs remains unknown. In view of the fact that size exerts a noteworthy influence on the electrochemical properties of many materials (Kim et al., 2005; Liu et al., 2005; Drezen et al., 2007; Wagemaker et al., 2007; Kiani et al., 2010; Jiang et al., 2017), understanding the effects of different sizes of MoS_2 on battery performance and electrochemical properties is important to application of MoS_2 in LIBs.

Herein, a hydro-refining technology combining crushing-grinding, flotation, mechanical exfoliation, and classification processes was developed to prepare a series of size-controlled MoS_2 sheets directly from natural raw molybdenite ore. This method is simple, eco-friendly, and high-yielding. When used the as-prepared MoS_2 sheets as LIB anodes, size displays an important effect on electrochemical properties. Among them, the MoS_2-1 μm electrode demonstrated excellent electrochemical properties with lower charge transfer resistance and rapider Li ions diffusion, delivering a higher specific capacity and initial coulombic efficiency. These results suggest the proper MoS_2 sheet size for LIBs and indicate the present approach is promising for industrial-scale production of natural molybdenite as high-capacity anodes.

MATERIALS AND METHODS

Materials

Natural raw ore (rock size: 5–10 cm, MoS_2 content: 1–2%) was received from China Molybdenum Co., Ltd. Raw ore was crushed to small stones (particle size ∼2 mm) and then ball-milled with water at a concentration of 66.6% to reduce the granularity. Ball-milled production, which is also called pulp (particle size: 75% <74 μm), was transferred to flotation cell, and water was added to adjust the concentration to 33%. In brief, 333 mg/L sodium silicate as depressant, 35 mg/L kerosene as molybdenite collector, and 15 mg/L terpineol as foaming agent were added sequentially to the pulp during agitation. Then, the pulp was aerated, and flotation froth was generated above the pulp and collected as the rough molybdenite concentrate (MoS_2 content: 2–5%), which then was reground to a fineness of 85% <37 μm by stirred mill. Finally, the reground rough concentrate was flotation cleaned eight times to improve the molybdenite concentrate grade. In the first cleaning operation, 2 g/L sodium sulfide was added to the pulp as the other sulfide minerals' depressant. Then, the obtained concentrate froth was transferred to the next cleaning operation, in which the sodium sulfide dosage was half of that used in the previous step. The final concentrate froth from the eighth cleaning operation was filtered and dried to achieve molybdenite concentrate (MoS_2 content: ∼92%).

Differently sized MoS_2 sheets were prepared through an intense shearing process. Molybdenite concentrate (10 g), polyvinylpyrrolidone-K30 (0.25 g, PVP-K30), and deionized water (500 mL) were placed in a stainless steel homogenizer. The homogenizer was run at 12,000 rpm for 5 h to exfoliate the molybdenite content and acquire a MoS_2 suspension. The homogeneous dispersion was gradient centrifuged at 1,000, 3,000, 5,500, and 10,000 rpm, and the precipitates were collected and rinsed by deionized water several times to remove the residual PVP. Afterward, the as-prepared differently sized MoS_2 sheets were dried at 60°C in a vacuum oven for 24 h.

Material Characterization

The crystal structure of the as-prepared materials was identified by X-ray diffraction (XRD, Bruker D8 diffractometer with monochromatic Cu Kα radiation and wavelength of 1.5406 Å). The composition of the samples was characterized by X-ray fluorescence (XRF). The particle size distribution was measured by laser diffraction (Malvern Mastersizer 2000). The morphology was analyzed by field emission scanning electron microscopy (FEI Quanta 200, Japan) and atomic force microscopy (AFM, Bruker Multimode V, Germany).

Electrochemical Characterization

The active materials, carboxymethyl cellulose, and conductive additive (Super P, carbon black) were mixed in a weight ratio

of 75:15:15 by using deionized water as the solvent. Then, the steady slurry was evenly painted on a copper foil. After drying at 80°C in a vacuum oven for 12 h, the copper foil was cut into wafer electrodes. The mass of the active material in each electrode was approximately 1.0 mg cm^{-2}. The CR2016 coin-type cells were assembled in an argon-filled glovebox (MBRAUN, Germany) by using as-prepared electrodes as the anode, metallic lithium disk as the counter electrode, and $LiClO_4$ (1 M) in ethylene carbonate and dimethyl carbonate (1:1, v/v) as the electrolyte. The capacities of Li-ion half cells were measured at different current densities in the voltage range of 0.01–3 V vs. Li^+/Li by using an Arbin battery testing system (BT2000). Cyclic voltammetry (CV) was performed by CHI660D electrochemical station (Shanghai Chenhua, China) in the voltage range of 0.01–3 V vs. Li^+/Li. Electrochemical impedance spectroscopy (EIS) was performed at the frequency range of 0.01 Hz to 100 kHz, and the excitation amplitude applied to the cells was 5 mV. All of the electrochemical tests were conducted at a temperature of 25°C.

RESULTS AND DISCUSSION

A schematic showing the hydro-refining process of preparing a series of size-controlled MoS_2 sheets directly from natural raw ore is illustrated in **Figure 1**. Initially, the particle size of natural raw ore is reduced by crushing and ball milling. Using flotation, molybdenite in the form of concentrate froth is separated from other nontarget minerals, and the recovery rate of molybdenite is ∼85%. The obtained molybdenite concentrate is further downsized by a homogenizer, which has a strong shearing force to exfoliate bulky molybdenite (i.e., MoS_2). Finally, the MoS_2 suspension is size-classified via high-speed gradient centrifugation. This method is low cost, environmental friendly, high-yielding, and is very promising for the large-scale preparation of MoS_2 sheets with various sizes.

The chemical composition of the natural raw ore and molybdenite concentrate is presented in **Table 1**. In natural raw ore, the dominant elements are O and Si, while the Mo content is only 0.82%, thus a facile and low-cost flotation process is indispensable to obtain pure molybdenite concentrate (Jiangang et al., 2012; Liu et al., 2012a). After flotation, the Mo content can reach to 55%, representing the high purity of the molybdenite concentrate. The slight oxidation of the natural molybdenite surface is due to the exposure to oxidative environment. The crystal structures and phases of the molybdenite concentrate and the differently sized MoS_2 are investigated by XRD (**Figure 2A**). All of these samples exhibit similar XRD patterns, which match well with the 2H MoS_2 phase (JCPDS no. 37-1492) (Ding et al., 2012; Xie et al., 2015; Sun et al., 2017). No extra peaks appear in the pattern, indicating their high purity, which agrees well with the XRF results. The peak at approximately 14.4° is the characteristic peak of (002) facet. Decreasing peak intensity and broadening peak width of (002) facet signify the thickness reduction of MoS_2 sheets (Wang et al., 2013d). Using the results from the XRD patterns, we calculate the grain parameters of each sample by the Scherrer equation:

$$D = K\lambda/\beta cos\theta \quad (1)$$

Where, D is the grain size, K is the Scherrer constant (0.89), λ is the diffraction light (X-ray) wavelength (0.15406 nm), β is the full width at half maximum, and θ is the Bragg angle. As shown in **Table 2**, the MoS_2-90 nm sample has the smallest grain size among them. Moreover, the volume average diameters of the samples are tested with a laser diffraction-based particle size analyzer. As shown in **Figure 2B**, the volume average diameters of the molybdenite concentrate and differently sized MoS_2 are 25.964, 5.346, 1.978, 1.023, and 0.092 μm, respectively.

The morphological of the samples are conducted by SEM and shown in **Figure 3**. **Figure 3A1** shows the morphology of the molybdenite concentrate where molybdenite particles exhibit various textures (flaky, blocky, and irregular shapes), and their size is mainly tens of microns, which can be attributed to the complex factors in natural mineralization. In addition, several small pieces of debris are found on the surface of large molybdenite particles with a size distribution from a few microns to submicron. From the higher-magnification observations, stacked compacted 2D layer structure is found distinctly in **Figures 3A2,A3**. By contrast, MoS_2-5 μm, MoS_2-2 μm, and MoS_2-1 μm show a lamellar morphology. As shown in **Figures 3B1–B3**, several thick sheets with size of ∼5 μm are distributed in the MoS_2-5 μm sample, which thickness is around 300 nm. Meanwhile, stratified structure and uneven edges are detected, accompanying with an increasing of active sites and defects. In the SEM images of MoS_2-2 μm and MoS_2-1 μm, small sheets with average sizes of ∼1 μm and ∼500 nm can be observed. The curved sheets shown in the higher-magnification images of **Figures 3C3,D3** indicate the thinness and flexibility of the MoS_2 sheets, which significantly ease the volume expansion during the charge and discharge cycles and enhance the stability of the batteries. **Figures 3E1,E2** show the compact agglomeration of nano-MoS_2 sheets in the MoS_2-90 nm sample, revealing the strong tendency of MoS_2 nanosheets to aggregate because of their high surface area and energy. This agglomeration dramatically decreases the active sites of the material and hinder Li^+ diffusion, which led to a low capacity. **Figure 3F** displays the compositions of molybdenite concentrate by energy disperse spectroscopy (EDS) analysis. No evident incidental element appears, and the atomic ratio of S to Mo is approximately 2, which further demonstrate the high purity of the molybdenite concentrate obtained from natural raw ore.

For exploring the crystalline characteristics of MoS_2 sample, TEM and HRTEM tests with various magnifications are performed. As shown in **Figures S1A,B**, thin sheets are detected in MoS_2-1 μm, accompanying with clear 2D layer structure. **Figure S1C** shows the HRTEM image of MoS_2-1 μm, revealing the abundant defects existing in MoS_2 sheets. Stripes spaced 0.273 nm apart in the insetmap are in good accordance with the (100) facet of MoS_2, as well as the single-crystal SAED pattern of MoS_2-1 μm shows the typical hexagonal spot pattern (**Figure S1D**). AFM tests are further carried out to obtain detailed information about the morphologies of MoS_2-5 μm, MoS_2-2 μm, MoS_2-1 μm, and MoS_2-90 nm. As shown in **Figures S2A2–C2**, the thickness of the MoS_2 sheets in the MoS_2-5 μm, MoS_2-2 μm, and MoS_2-1 μm samples gradually decrease from ∼330 to ∼170 nm and then to ∼100 nm. The same trend is observed

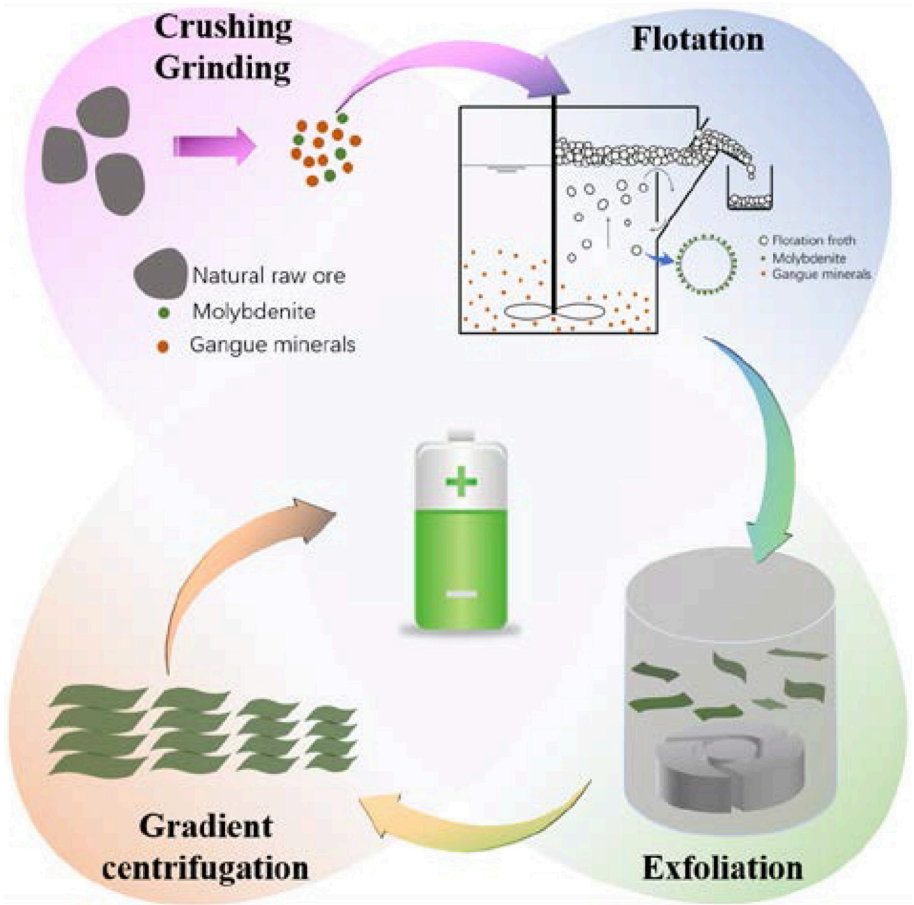

FIGURE 1 | Schematic plan of hydro-refining process of natural raw ore.

TABLE 1 | Chemical composition of natural raw ore and molybdenite concentrate.

Element (wt %)	Mo	S	O	Fe	Si
Natural raw ore	0.82	0.48	46.21	1.56	30.66
Molybdenite concentrate	55.61	40.00	2.140	0.15	0.016

for the sheet diameter (**Figures S2A1–C1**). Stratified structures and rough edges can also be observed in the 3D plots (**Figures S2A3–C3**), indicating more active sites can be exposed for Li ions. The image of the MoS_2-90 nm sample shown in **Figure S2D1** displays three irregular particles with a thickness of ∼230 nm and a diameter of ∼1 μm. Similar to the SEM results, the AFM findings indicate that these uncommon particles are the agglomeration of nano-MoS_2 sheets. When observing at a small height scale, two pieces of thin films are visible with a thickness of ∼0.65 nm, indicating single-layer MoS_2 films distributing in the MoS_2-90 nm sample.

The electrochemical properties of the as-prepared samples are measured by galvanostatic charge–discharge test at various current densities. **Figure 4A** shows the initial charge and discharge curves of molybdenite concentrate and MoS_2 samples at 100 mA g^{-1}, where two potential plateaus at approximately 1.1 and 0.6 V vs. Li/Li^+ in the first discharge (lithiation) of the electrodes are observed. The first plateau at 1.1 V could be attributed to the intercalation of Li^+ into MoS_2 interlayers ($MoS_2 + xLi^+ + xe^- \rightarrow Li_xMoS_2$), and the low plateau at 0.6 V is due to the conversion reaction of Li_xMoS_2 to Mo metal and Li_2S ($Li_xMoS_2 + (4 - x)Li^+ + (4 - x)e^- \rightarrow Mo + 2Li_2S$). Only one significant potential plateau at approximately 2.3 V appeared in the first charge (delithiation) process, and it corresponds to the delithiation of Li_2S ($Li_2S - 2e^- \rightarrow 2Li^+ + S$). This result demonstrates that the conversion reaction is irreversible (Xiao et al., 2010; Stephenson et al., 2014). The electrochemical behavior is further analyzed by CV (**Figure 4B**). In the first cathodic sweep, two peaks appear at approximately 0.93 and 0.23 V, which are attributed to the insertion and conversion reactions, respectively. Meanwhile, these two peaks weaken in subsequent cathodic cycles. Instead, a sharp reduction peak arises at approximately 1.84 V, which matches well with the behavior in Li-S battery and corresponds to the reaction of S to Li_2S (Ji and Nazar, 2010; Elazari et al., 2011). In the anodic sweep, one shallow peak at 1.69 V and one sharp peak at 2.33 V are observed. The first oxidation peak is due to the delithiation of residual Li_xMoS_2, and the latter peak represents

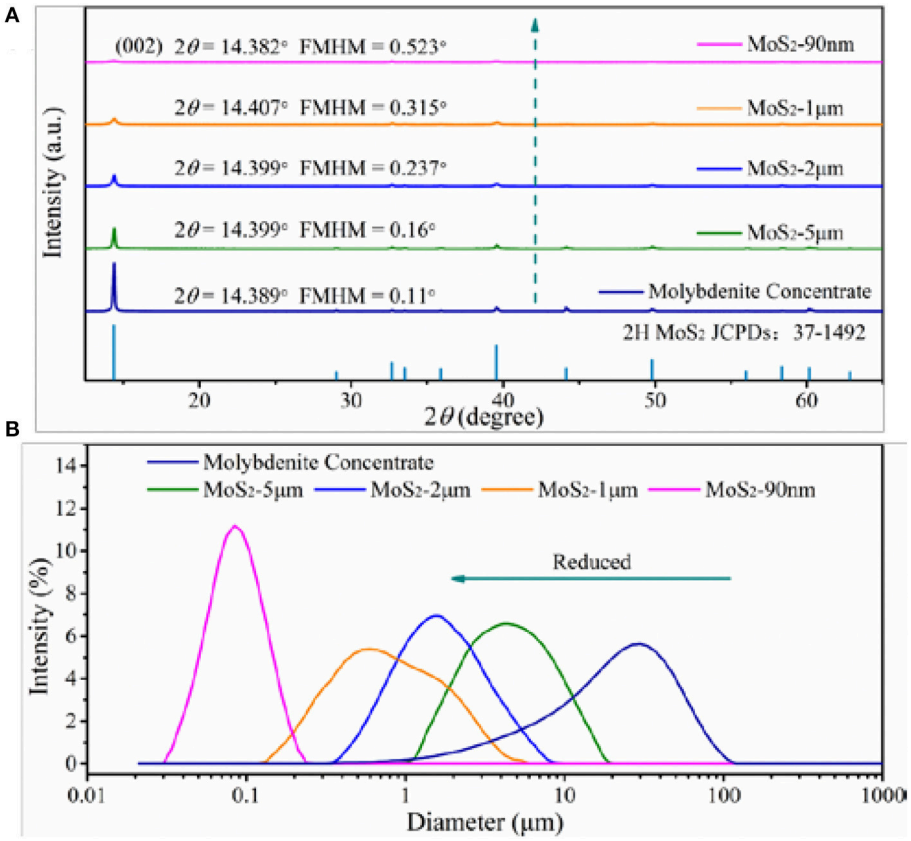

FIGURE 2 | (A) XRD spectra of molybdenite concentrate and MoS_2 samples. **(B)** Particle size analysis of molybdenite concentrate and MoS_2 samples.

TABLE 2 | Crystal parameters of molybdenite concentrate and MoS_2 samples.

	Molybdenite concentrate	MoS_2-5 μm	MoS_2-2 μm	MoS_2-1 μm	MoS_2-90 nm
2θ (deg)	13.389	14.399	14.399	14.407	14.382
β (rad)	0.0019	0.0028	0.0041	0.0055	0.0091
D (nm)	70.34	48.36	32.65	24.56	14.79

the conversion of Li_2S to S (Song et al., 2013; Stephenson et al., 2014).

As shown in **Figure 4A**, the initial discharge specific capacities of molybdenite concentrate, MoS_2-5 μm, MoS_2-2 μm, MoS_2-1 μm, and MoS_2-90 nm are 688, 779, 868, 1134, and 1004 mAh g^{-1} at 100 mA g^{-1}, respectively, while the initial charge capacities are 589, 653, 555, 904, and 611 mAh g^{-1}. Among them, the MoS_2-1 μm has a higher capacity owing to its compared richer active sites. **Figure 4C** shows the cycling performance of the molybdenite concentrate and MoS_2 samples at 100 mA g^{-1}. The molybdenite concentrate exhibits an unsatisfied stability, which capacity gradually decreases to 217 mAh g^{-1} after 125 cycles, showing a low capacity retention of 37%. MoS_2-5 μm displays a specific capacity of ∼600 mAh g^{-1} before 50 cycles with no evident fading, while fades quickly to 355 mAh g^{-1}. The poor cycling stabilities of the molybdenite concentrate and MoS_2-5 μm can be ascribed to the large volume expansion of bulk MoS_2 during repeated charge/discharge processes, causing the harmful shedding of active materials. Meanwhile, MoS_2-2 μm, MoS_2-1 μm, and MoS_2-90 nm show excellent stability without any capacity decay. As shown, the capacities of MoS_2-2 μm, MoS_2-1 μm, and MoS_2-90 nm increase with the cycling going on, reaching up to 1013, 1337, and 881 mAh g^{-1} after 125 cycles. The data reported here are higher than most of the reported works (**Table 3**). The promotion in capacity may be attributed to the increased Mo atoms created by the irreversible redox reaction during repeated charge/discharge processes, bringing about better conductivity. Meanwhile, Mo atoms accommodate a large amount of Li ions over prolonged discharging process, increasing the electrode's Li-capacity. The significant differences between these prepared samples indicate that decreasing the particle size of MoS_2 can significantly improve the cycling stability and capacity of batteries due to the stronger and more flexible structure and more active spots. However, MoS_2-90 nm displays a lower capacity than MoS_2-1 μm may due to the particle agglomeration, accompanying with the reduction in active spots.

Figure 4D shows the coulombic efficiencies of the MoS_2 samples at 100 mA g^{-1}. The initial coulombic efficiencies of MoS_2-5 μm, MoS_2-2 μm, MoS_2-1 μm, and MoS_2-90 m are 83.9, 63.9, 79.7, and 60.9%, respectively, which rapidly increase to

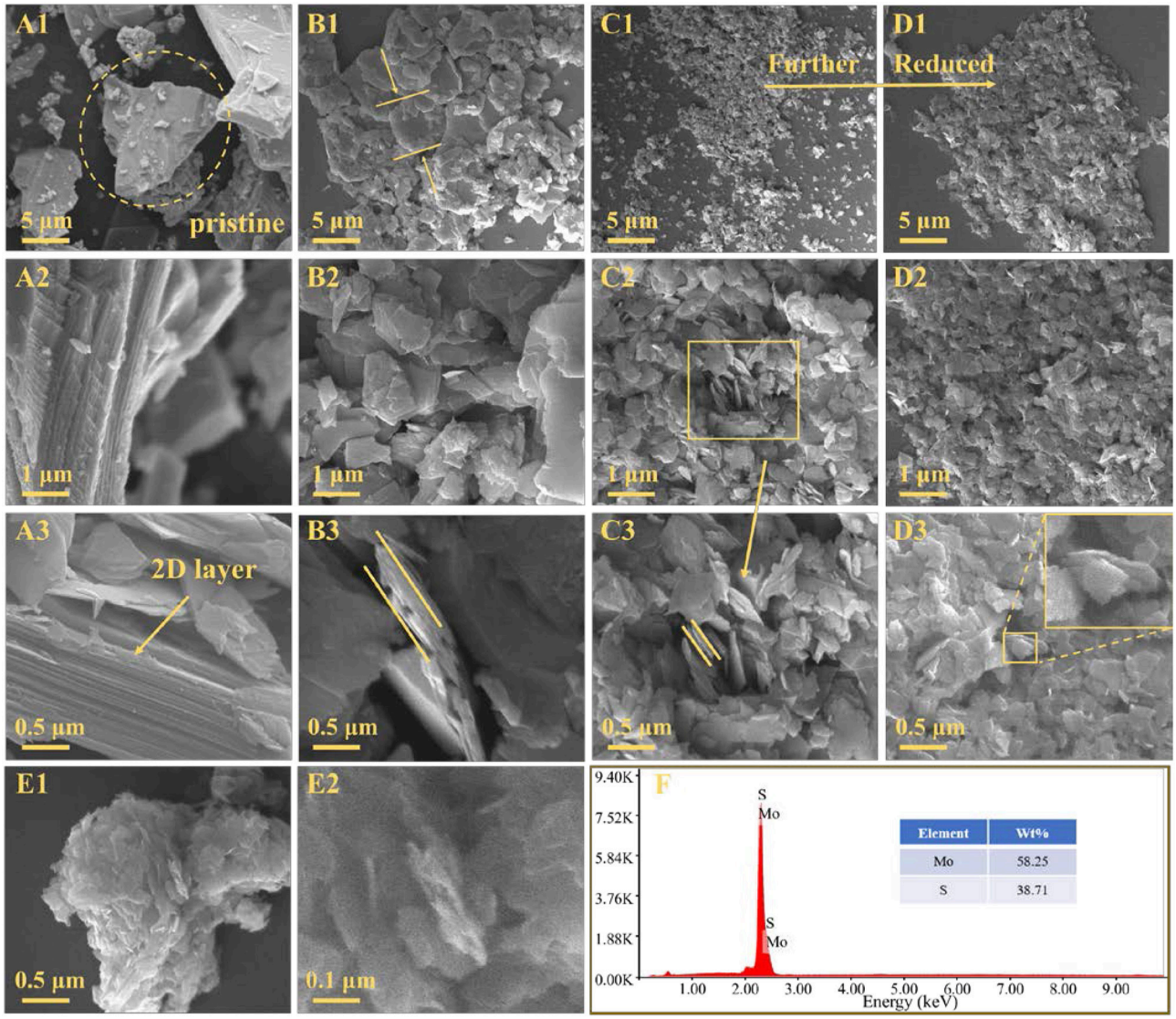

FIGURE 3 | SEM images of **(A1–A3)** molybdenite concentrate, **(B1–B3)** MoS_2-5 μm, **(C1–C3)** MoS_2-2 μm, **(D1–D3)** MoS_2-1 μm and **(E1, E2)** MoS_2-90 nm. **(F)** Energy-dispersive spectrometry (EDS) of molybdenite concentrate.

>97% after five cycles. The significant difference in initial coulombic efficiency between MoS_2 samples can be explained through the electrochemical behavior during the first lithiation process. Unlike the conversion reaction, Li ion intercalation is a reversible reaction. Thus, a high ratio of intercalation capacity can result in a high initial coulomb efficiency. As shown in **Figure 4E**, the intercalation capacity ratios of MoS_2-5 μm, MoS_2-2 μm, MoS_2-1 μm, and MoS_2-90 m are calculated to be 23.06, 9.06, 23.05, and 8.26%, respectively, which correspond well to the initial coulombic efficiencies. Moreover, the initial coulombic efficiency is an important parameter that determines the industrial application feasibility of electrode materials. Individual MoS_2-5 μm and MoS_2-1 μm have much higher initial coulombic efficiencies, suggesting that they are more conducive to the application of full batteries than MoS_2-2 μm and MoS_2-90 nm.

The galvanostatic charge and discharge profiles of four MoS_2 electrodes at 100 mA g^{-1} are shown in **Figures 4F–I**. **Figure 4H** shows that, different from the initial discharge curve, a new potential plateau emerges at 2.0 V vs. Li/Li^+, and the two aforementioned potential plateaus at 1.1 and 0.6 V disappear in the second discharge profile. This appearance indicates that the dominant reaction of the discharge process turns into S lithiation ($S + 2Li^+ + 2e^- \rightarrow Li_2S$) (Chang et al., 2013; Zhu et al., 2014), which is in good accordance with the aforementioned CV results. **Figure 4F,G,I** show the charge and discharge curves of the three other electrodes, which are similar to that of the MoS_2-1 μm electrode.

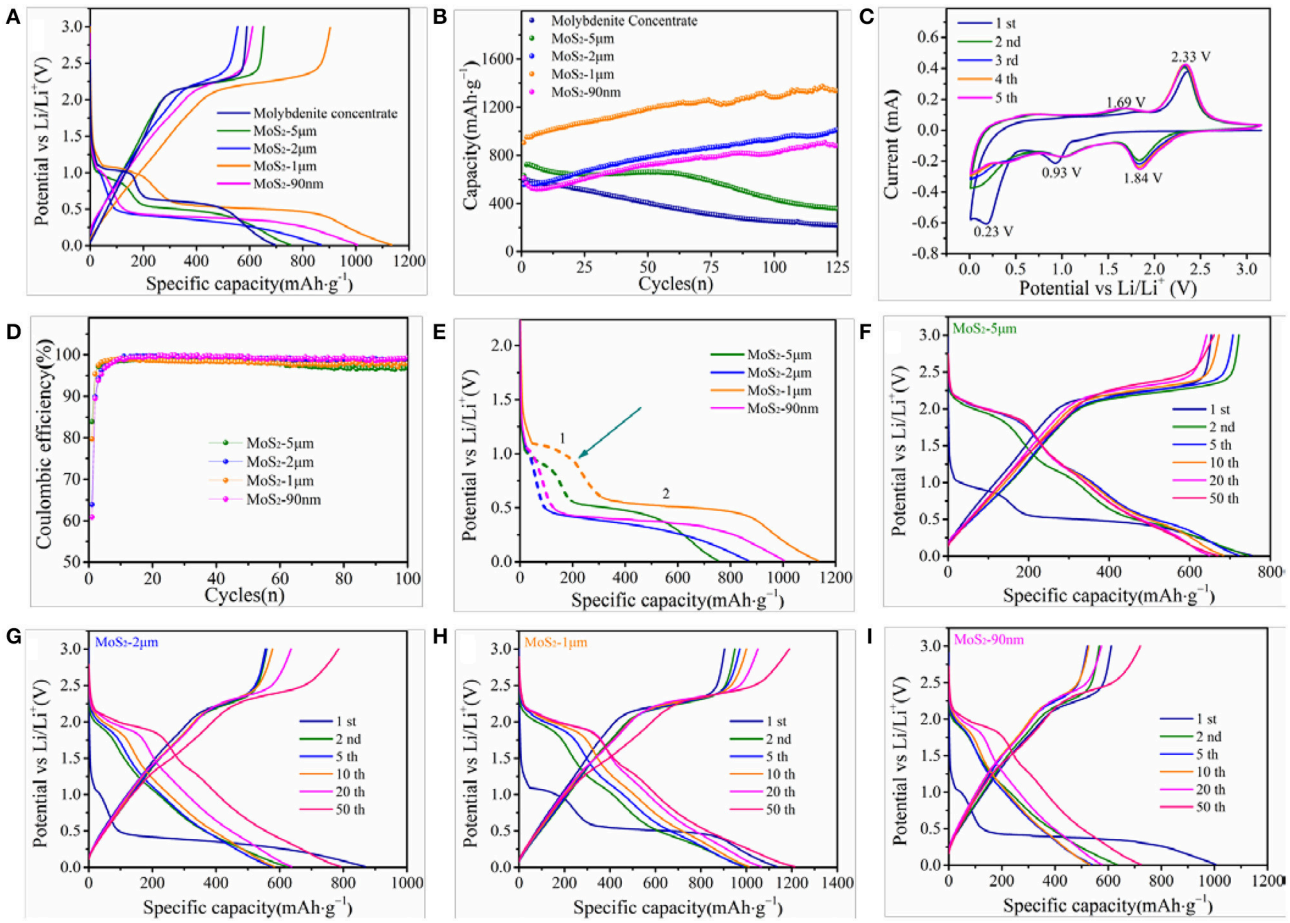

FIGURE 4 | (A) Initial charge and discharge curves of molybdenite concentrate and MoS_2 samples at 100 mA g^{-1}. **(B)** CV curves of the MoS_2-1 μm electrode for the initial 5 cycles at a scanning rate of 0.2 mV s^{-1}. **(C)** Cycling performance of molybdenite concentrate and MoS_2 samples at 100 mA g^{-1}. **(D)** Coulombic efficiency of MoS_2 samples at 100 mA g^{-1}. **(E)** Discharge curves of MoS_2 samples in the first cycle. Galvanostatic charge and discharge profiles of **(F)** MoS_2-5 μm, **(G)** MoS_2-2 μm, **(H)** MoS_2-1 μm and **(I)** MoS_2-90 nm electrodes at 100 mA g^{-1}.

Figure 5A shows the rate performances of MoS_2-5μm, MoS_2-2μm, MoS_2-1μm, and MoS_2-90nm. Apparently, the capacity of MoS_2-1μm is much higher than those of MoS_2-5μm, MoS_2-2μm, and MoS_2-90nm. The charge capacities of the MoS_2-1μm anode at 0.5, 1.0, 2.0, and 5.0 A g^{-1} are 931, 900, 857, and 682 mAh g^{-1}, respectively. When the current density reverts to 0.1 A g^{-1}, the capacity recovers to a high value of 1,239 mAh g^{-1}, indicating the strong tolerance of the electrode for the rapid charge–discharge process and the remarkable capacity recoverability of the MoS_2-1 μm electrode. Meanwhile, the charge capacities of MoS_2-5 μm are 516, 464, and 342 mAh g^{-1} at 0.5, 1.0, 2.0, and 5.0 A g^{-1}, respectively, and then reverts to 597 mAh g^{-1} at 0.1 A g^{-1}, which is close to the initial capacity. However, along with increasing loops, the capacity declines following a similar pattern to the previous result. The charge capacities of MoS_2-2 μm and MoS_2-90 nm are 355 and 217 mAh g^{-1} at 1.0 A g^{-1} and 146 and 76 mAh g^{-1} at 5.0 A g^{-1}, respectively, which are unsatisfactory. **Figures 5B–E** display the comparation of the charge and discharge curves of MoS_2-5 μm, MoS_2-2 μm, MoS_2-1 μm, and MoS_2-90 nm at various current densities. As shown in **Figure 5E**, the MoS_2-1 μm electrode keeps a similar charge and discharge curves even at a high current density, as well as considerable capacity retention, further revealing its excellent rate performance. While for MoS_2-5 μm, MoS_2-2 μm, and MoS_2-90 nm, it is difficult for them to maintain the original charge and discharge behavior at high current densities, leading to a sharp declining in capacity (**Figures 5B,C,F**).

To confirm the difference in electrochemical performance of the differentially expressed MoS_2, EIS tests are performed to analyze the electronic conductivity and ion diffusion rate of the samples. **Figure 6A** shows the Nyquist plots at fully uncharged-undischarged state, accompanied by fitted equivalent circuit. The semicircular loop at the high-middle frequencies is related to the resistance of solid electrolyte interface and charge transfer resistance (R_{ct}), while the slope line at low frequencies represents the Warburg impedance, which is connected to Li ion diffusion of the electrode materials(Wang et al., 2013a).

TABLE 3 | Composition of this work and other previous reported results.

Electrode material	Method	Morphology	Reserved capacity (mAh g^{-1}) after (Y) cycles at (Z) current density	References
MoS_2	Hydrothermal	Nanoflakes	780 (40) (0.04 A g^{-1})	Feng et al., 2009
MoS_2	Impregnation	Wire-like Arrays	876 (100) (0.1 A g^{-1})	Liu et al., 2012b
MoS_2	Hydrothermal	3D Flower-like Spheres	947 (50) (0.1 A g^{-1})	Yang et al., 2014
MoS_2	Solution Process	Restacked Nanosheets	750 (50) (0.05 A g^{-1})	Du et al., 2010
MoS_2	Hydrothermal	Hollow Nanoparticles	902 (80) (0.1 A g^{-1})	Wang et al., 2013c
Molybdenite	Hydro-refining	**Nanosheets**	**1337 (125) (0.1 A g^{-1})**	**This work**

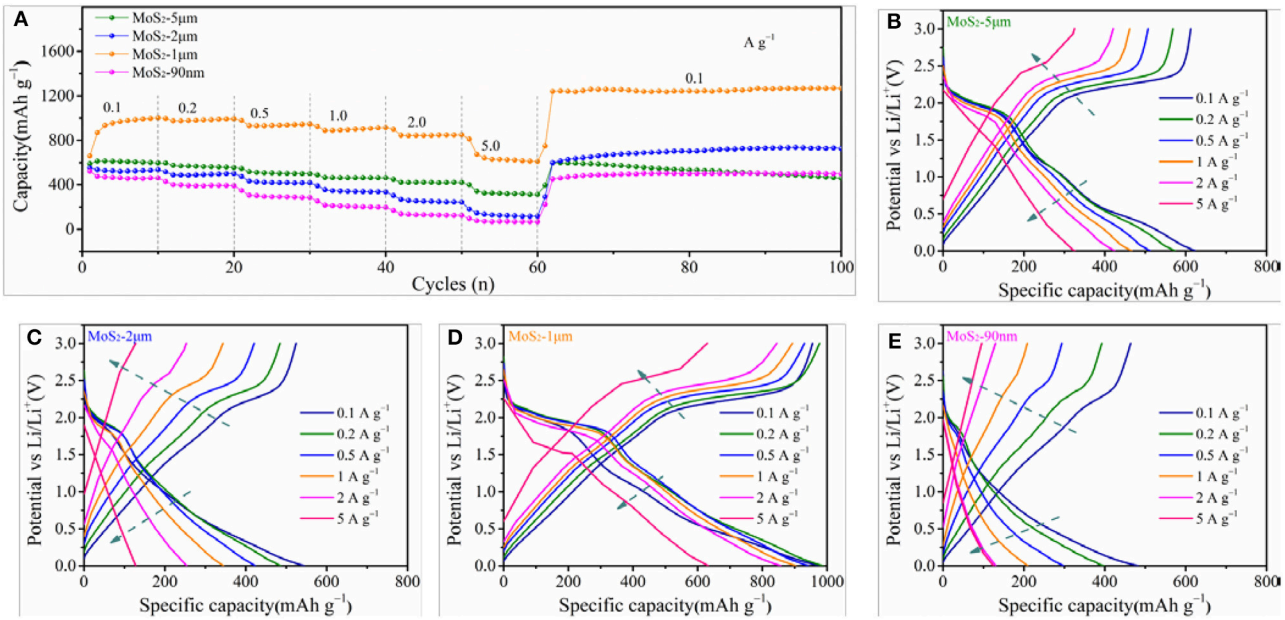

FIGURE 5 | (A) Rate performance of MoS_2 samples at various current densities. Comparation of the charge and discharge curves of **(B)** MoS_2-5 μm, **(C)** MoS_2-2 μm, **(D)** MoS_2-1 μm, and **(E)** MoS_2-90 nm at various current densities.

The smaller semicircle of MoS_2-1 μm compared with MoS_2-5 μm, MoS_2-2 μm, and MoS_2-90 nm indicates a lower R_{ct}. Thus, MoS_2-1 μm is more conducive to charge transfer compared with the other samples (Jiang et al., 2017). **Figure 6D** shows the relationship between Z_r and negative square root of angular frequency ($\omega^{-1/2}$) in the low-frequency region at fully uncharged–undischarged state. Using the slope of the fitted line (Warburg coefficient), the Li ion diffusion coefficient can be calculated according to the following equation (Wu et al., 2016, 2017; Li et al., 2018):

$$D_{Li^+} = 0.5R^2T^2/A^2n^4F^4C^2\sigma^2 \quad (2)$$

where $D_{Li}+$ is the Li ion diffusion coefficient, R is the gas constant (8.314 J mol^{-1} K^{-1}), T is the absolute temperature (298 K), A is the area of the electrode (1.53 cm^2), n is the transfer electrons (for Li^+, $n = 1$), F is the Faraday constant (96,485 C mol^{-1}), C is the Li ion lattice concentration (0.001 mol cm^{-2}), and σ is the Warburg coefficient. As shown in **Figure 6G**, at fully uncharged–undischarged state, the $D_{Li}+$ values of MoS_2-5 μm, MoS_2-2 μm, MoS_2-1 μm, and MoS_2-90 nm are 7×10^{-15}, 4.68×10^{-15}, 7.56×10^{-13}, and 3.21×10^{-15} cm^2 s^{-1}, respectively. Apparently, the Li ion diffusion coefficient of MoS_2-1 μm is two orders of magnitude larger than those of the three other samples, which can reflect the higher initial capacity of MoS_2-1μm (**Figure 4C**).

Figures 6B,E show the Nyquist plots at initially discharged to 1.1 V vs. Li/Li^+ state where Li ion intercalation occurs and the corresponding relationship between Z_r and $\omega^{-1/2}$. The semicircles of MoS_2-1 μm and MoS_2-5 μm are smaller than those of MoS_2-2 μm, and MoS_2-90 nm, respectively. Thus, R_{ct} is lower and charge transfer is much easier for MoS_2-1 μm and MoS_2-5 μm than for MoS_2-2 μm and MoS_2-90 nm. The calculated $D_{Li}+$ values of MoS_2-5 μm, MoS_2-2 μm, MoS_2-1 μm, and MoS_2-90 nm at initially discharged to 1.1 V vs. Li/Li^+ state are 2.46×10^{-13}, 2.19×10^{-15}, 4.80×10^{-13}, and 5.43×10^{-14} cm^2 s^{-1}, respectively (**Figure 6H**). On the basis of the results of R_{ct} and $D_{Li}+$, the intensities of the Li ion intercalation can be ranked as MoS_2-1 μm > MoS_2-5 μm > MoS_2-90 nm > MoS_2-2 μm. As shown in **Figure 6C**, the semicircles of Nyquist plots, which at initially discharged to 0.6 V vs. Li/Li^+ state

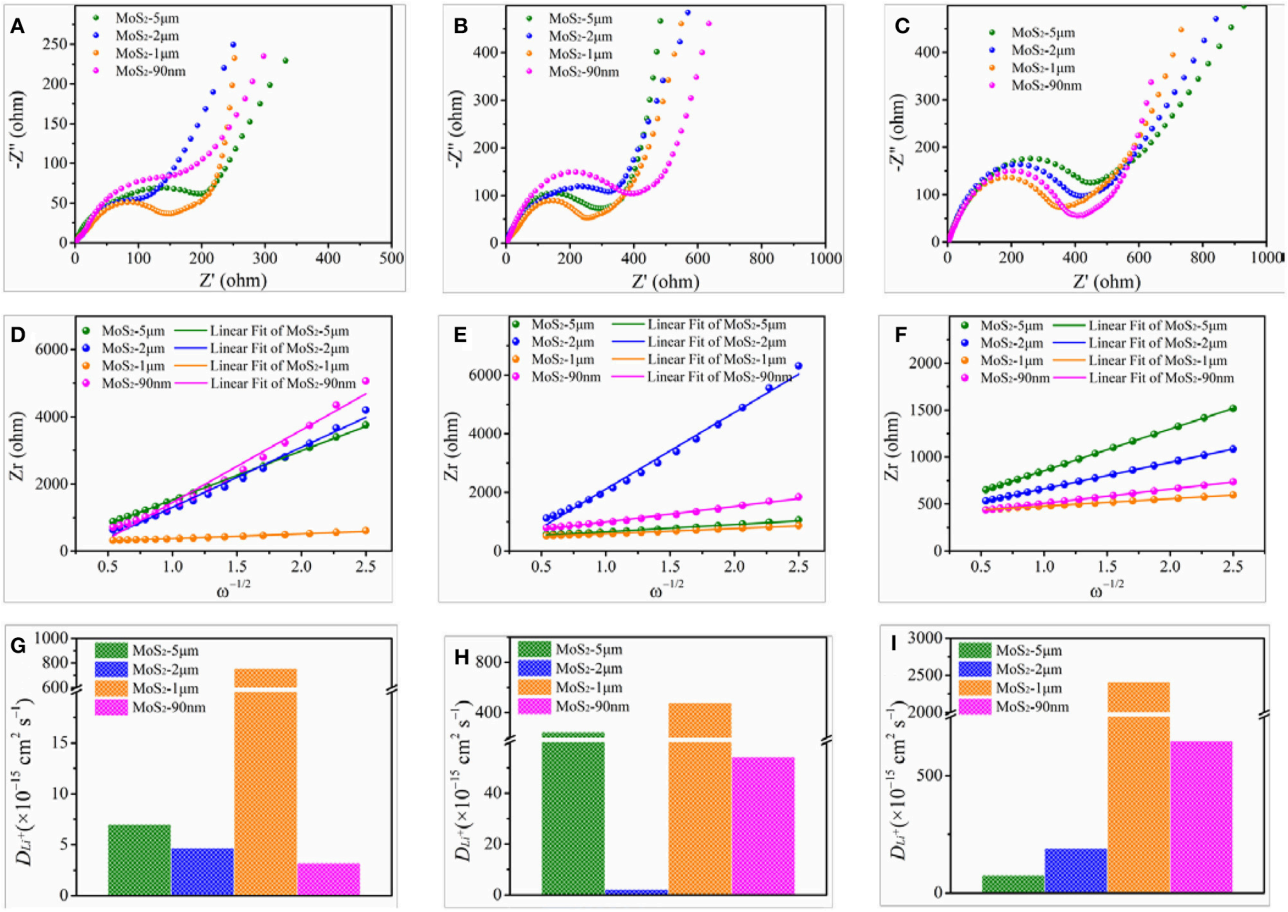

FIGURE 6 | EIS curves of MoS_2 samples at **(A)** fully uncharged/undischarged state, **(B)** first discharged to 1.1 V vs. Li/Li^+ state, **(C)** first discharged to 0.6 V vs. Li/Li^+ state. **(D–F)** The corresponding relationship between Zr and negative square root of angular frequency ($\omega^{-1/2}$) at various states. **(G–I)** The corresponding Li ion diffusion coefficient ($D_{Li}+$) of MoS_2 samples at various states.

where conversion reaction occurs, gradually enlarge from MoS_2-1 μm to MoS_2-5 μm. Simultaneously, the calculated $D_{Li}+$ values for MoS_2-5 μm, MoS_2-2 μm, MoS_2-1 μm, and MoS_2-90 nm are 7.66×10^{-14}, 1.9×10^{-13}, 2.41×10^{-12}, and 6.47×10^{-13} $cm^2\ s^{-1}$, respectively (**Figure 6I**). These results indicate the significantly stronger conversion reactions of MoS_2-1 μm than other samples.

CV tests are conducted to further investigate the electrochemical kinetics of the as-prepared samples. **Figures 7A,B,D,E** show the CV curves of the MoS_2 samples at different scanning rates, where the four MoS_2 samples display similar CV behaviors. The dominant oxidation and reduction peaks appear at approximately 2.48 and 1.80 V vs. Li/Li^+, respectively. Moreover, the peak at 2.48 V splits into two parts, which agrees well with the gradient conversion from element S_8 to polysulfides and then to Li_2S (Xiao et al., 2011). As the scan rate increasing, the peak current elevates, and the oxidation peak potential shifts positively while the reduction peak potential toward negatively. As shown in **Figure 7G**, the peak intensities clearly show the following trend: MoS_2-1 μm > MoS_2-5 μm > MoS_2-90 nm > MoS_2-2 μm, indicating the largest capacity of MoS_2-1 μm electrode (Chou et al., 2011). **Figures 7C,F** show the relationship between the peak current and square root of scan rate ($v^{1/2}$), which can be expressed by the following equation (Wang et al., 2013b; Sun et al., 2017):

$$i_p = 2.69 \times 10^5 n^{\frac{3}{2}} A D^{\frac{1}{2}} v^{\frac{1}{2}} C_0 \quad (3)$$

where i_p is the peak current, v is the scan rate, n is the transfer electrons (for Li^+ $n = 1$), A is the area of the electrode (1.53 cm^2), D is the Li ion diffusion coefficient, and ΔC_0 is the change in Li^+ concentration in the electrochemical reaction. Ion diffusion is a rate-determining step in the electrode. Thus, when scanning at a slow rate (<1 mV s^{-1}), the peak current (i_p) varied linearly with the square root of scan rate ($v^{1/2}$). Hence, the slope can be utilized to characterize the Li ion diffusion coefficient (D). The results suggest that the fitting line slope of MoS_2-1 μm is higher than that of the other samples (**Figure 7H**), revealing that MoS_2-1 μm has better Li ion diffusion rate than the other samples, which is in good accordance with the EIS test results.

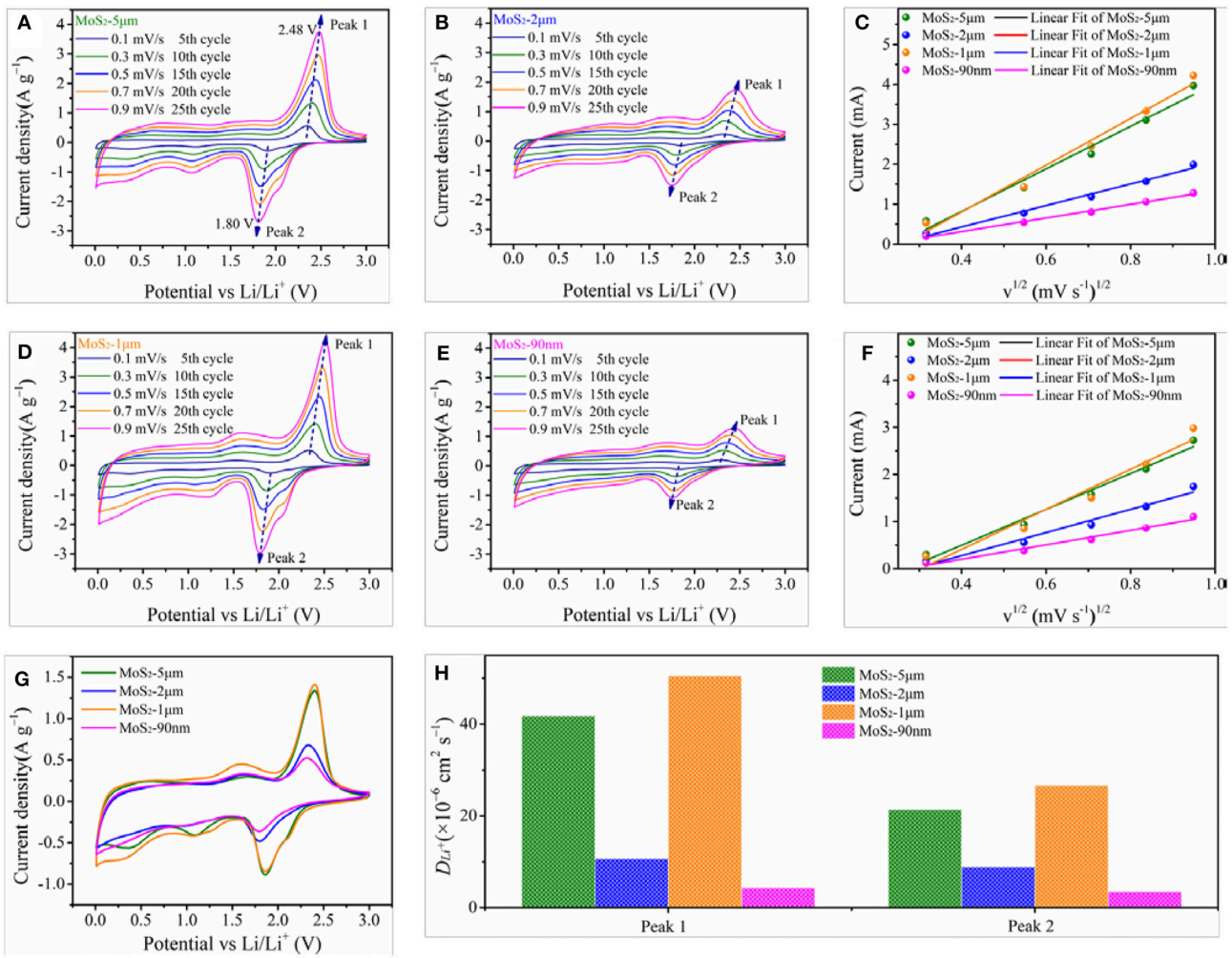

FIGURE 7 | CV curves of **(A)** MoS_2-5 μm, **(B)** MoS_2-2 μm, **(D)** MoS_2-1 μm and **(E)** MoS_2-90 nm at various scanning rates from 0.1 to 0.9 mV s^{-1}. The relationship between the peak current and square root of scan rate (v1/2) of **(C)** oxidation peak (Peak 1), **(F)** reduction peak (Peak 2). **(G)** Comparation of CV curves of MoS2 samples at 0.9 mV s^{-1}. **(H)** Li ion diffusion coefficient (D_{Li}+) of Peak 1 and Peak 2.

CONCLUSIONS

Herein, 2D MoS_2 sheets were successfully prepared from abundant natural raw molybdenite ore by a low-cost, environmental-friendly and high-yielding hydro-refining technology, containing crushing–grinding, flotation, physical exfoliation, and gradient centrifugation. Furthermore, the efficient tailoring and classification processes realized a series of size-controlled (5μm, 2μm, 1μm, 90nm) MoS_2 sheets to improve Li-capacity and stability. When used as LIB anodes, size displayed significant effects on electrochemical performance. The MoS_2-1 μm electrode demonstrated a higher initial charge capacity of 904 mAh g^{-1}, further increasing to 1,337 mAh g^{-1} over 125 cycles at 0.1 A g^{-1}. The excellent rate performance of the MoS_2-1 μm electrode showed considerable capacities of 857 and 682 mAh g^{-1} at 2.0 and 5.0 A g^{-1}, respectively. Owing to extraordinary morphology brought from tailoring craft, the as-prepared sheets offering rich active sites and defects for interacting with Li ions. Meanwhile, flexible structure could relieve volume expansion, significantly promoting the cycling stability. What's more, in-depth electrochemical kinetic analysis disclosed that the MoS_2-1 μm electrode shows a lower charge transfer resistance and higher Li ion diffusion coefficient at various states, resulted from the successful size-tuning process. This work presents the remarkable effect of different MoS_2 sheet sizes on Li-storage performance and provides a promising strategy for the large-scale production of MoS_2-based LIB anodes from natural molybdenite mineral.

AUTHOR CONTRIBUTIONS

FJ conducted the experiments. WS and XJ are the supervisor of this research work. SL, PG, and SK helped writing. HT and

HH helped operating experiments. FJ, SL, HT, CZ, YY and YH performed the characterization and data analysis. All authors involved the analysis of experimental data and manuscript preparation.

FUNDING

This research was financially supported by the National 111 Project (B14034), collaborative Innovation Center for Clean and Efficient Utilization of Strategic Metal Mineral Resources, Found of State Key Laboratory of Mineral Processing (BGRIMM-KJSKL-2017-13), National Natural Science Foundation of China (51374247, 51704330, 51622406, 21673298 and 21473258), National Key Research and Development Program of China (2017YFB0102000), Scientific Research Starting Foundation of Central South University (202045006).

SUPPLEMENTARY MATERIAL

The Supplementary Material for this article can be found online at: https://www.frontiersin.org/articles/10.3389/fchem.2018.00389/full#supplementary-material

REFERENCES

Acerce, M., Voiry, D., and Chhowalla, M. (2015). Metallic 1T phase MoS_2 nanosheets as supercapacitor electrode materials. *Nat. Nanotech.* 10, 313–318. doi: 10.1038/nnano.2015.40

Altavilla, C., Sarno, M., and Ciambelli, P. (2011). A novel wet chemistry approach for the synthesis of hybrid 2D free-floating single or multilayer nanosheets of MS_2@oleylamine (M - Mo, W). *Chem. Mater.* 23, 3879–3885. doi: 10.1021/cm200837g

Chang, K., Geng, D., Li, X., Yang, J., Tang, Y., Cai, M., et al. (2013). Ultrathin MoS_2/nitrogen-doped graphene nanosheets with highly reversible lithium storage. *Adv. Energy Mater.* 3, 839–844. doi: 10.1002/aenm.201201108

Chhowalla, M., Shin, H. S., Eda, G., Li, L. J., Loh, K. P., and Zhang, H. (2013). The chemistry of two-dimensional layered transition metal dichalcogenide nanosheets. *Nat. Chem.* 5, 263–275. doi: 10.1038/nchem.1589

Chou, S. L., Gao, X. W., Wang, J. Z., Wexler, D., Wang, Z. X., Chen, L. Q., et al. (2011). Tin/polypyrrole composite anode using sodium carboxymethyl cellulose binder for lithium-ion batteries. *Dalton Trans.* 40, 12801–12807. doi: 10.1039/c1dt10396b

Dankert, A., Langouche, L., Kamalakar, M. V., and Dash, S. P. (2014). High-performance molybdenum disulfide field-effect transistors with spin tunnel contacts. *ACS Nano* 8, 476–482. doi: 10.1021/nn404961e

Ding, S., Zhang, D., Chen, J. S., and Lou, X. W. (2012). Facile synthesis of hierarchical MoS_2 microspheres composed of few-layered nanosheets and their lithium storage properties. *Nanoscale* 4, 95–98. doi: 10.1039/C1NR11552A

Drezen, T., Kwon, N. H., Bowen, P., Teerlinck, I., Isono, M., and Exnar, I. (2007). Effect of particle size on $LiMnPO_4$ cathodes. *J. Power Sources* 174, 949–953. doi: 10.1016/j.jpowsour.2007.06.203

Du, G., Guo, Z., Wang, S., Zeng, R., Chen, Z., and Liu, H. (2010). Superior stability and high capacity of restacked molybdenum disulfide as anode material for lithium ion batteries. *Chem. Commun.* 46, 1106–1108. doi: 10.1039/B920277C

Elazari, R., Salitra, G., Garsuch, A., Panchenko, A., and Aurbach, D. (2011). Sulfur-impregnated activated carbon fiber cloth as a binder-free cathode for rechargeable Li-S batteries. *Adv. Mater.* 23, 5641–5644. doi: 10.1002/adma.201103274

Feng, C., Ma, J., Li, H., Zeng, R., Guo, Z., and Liu, H. (2009). Synthesis of molybdenum disulfide (MoS2) for lithium ion battery applications. *Mat. Res. Bull.* 44, 1811–1815. doi: 10.1016/j.materresbull.2009.05.018

Gao, M. R., Chan, M. K., and Sun, Y. (2015a). Edge-terminated molybdenum disulfide with a 9.4-A interlayer spacing for electrochemical hydrogen production. *Nat. Commun.* 6:7493. doi: 10.1038/ncomms8493

Gao, M. R., Liang, J. X., Zheng, Y. R., Xu, Y. F., Jiang, J., Gao, Q., et al. (2015b). An efficient molybdenum disulfide/cobalt diselenide hybrid catalyst for electrochemical hydrogen generation. *Nat. Commun.* 6:5982. doi: 10.1038/ncomms6982

Ge, P., Hou, H., Ji, X., Huang, Z., Li, S., and Huang, L. (2018a). Enhanced stability of sodium storage exhibited by carbon coated Sb_2S_3 hollow spheres. *Mater. Chem. Phys.* 203, 185–192. doi: 10.1016/j.matchemphys.2017.10.003

Ge, P., Zhang, C., Hou, H., Wu, B., Zhou, L., Li, S., et al. (2018b). Anions induced evolution of Co_3X_4 (X = O, S, Se) as sodium-ion anodes: The influences of electronic structure, morphology, electrochemical property. *Nano Energy* 48, 617–629. doi: 10.1016/j.nanoen.2018.04.018

Geng, X., Sun, W., Wu, W., Chen, B., Al-Hilo, A., Benamara, M., et al. (2016). Pure and stable metallic phase molybdenum disulfide nanosheets for hydrogen evolution reaction. *Nat. Commun.* 7:10672. doi: 10.1038/ncomms10672

Hai, N. Q., Kwon, S. H., Kim, H., Kim, I. T., Lee, S. G., and Hur, J. (2018). High-performance MoS_2 -based nanocomposite anode prepared by high-energy mechanical milling: the effect of carbonaceous matrix on MoS_2. *Electrochim. Acta* 260, 129–138. doi: 10.1016/j.electacta.2017.11.068

Ji, X., and Nazar, L. F. (2010). Advances in Li–S batteries. *J. Mater. Chem.* 20, 9821–9826. doi: 10.1039/b925751a

Jiang, X., Zhang, T., and Lee, J. Y. (2017). Does size matter–What other factors are limiting the rate performance of $Na_3V_2(PO_4)_3$ cathode in sodium-ion batteries. *J. Power Sources* 372, 91–98. doi: 10.1016/j.jpowsour.2017.10.075

Jiangang, F., Kaida, C., Hui, W., Chao, G., and Wei, L. (2012). Recovering molybdenite from ultrafine waste tailings by oil agglomerate flotation. *Miner. Eng.* 39, 133–139. doi: 10.1016/j.mineng.2012.07.006

Kiani, M. A., Mousavi, M. F., and Ghasemi, S. (2010). Size effect investigation on battery performance: comparison between micro- and nano-particles of β-$Ni(OH)_2$ as nickel battery cathode material. *J. Power Sources* 195, 5794–5800. doi: 10.1016/j.jpowsour.2010.03.080

Kim, C., Noh, M., Choi, M., Cho, J., and Park, B. (2005). Critical size of a nano SnO_2 electrode for Li-secondsary battery. *Chem. Mater.* 17, 3297–3301. doi: 10.1021/cm048003o

Li, Q., Zhang, N., Yang, Y., Wang, G., and Ng, D. H. (2014). High efficiency photocatalysis for pollutant degradation with MoS_2/C_3N_4 heterostructures. *Langmuir* 30, 8965–8972. doi: 10.1021/la502033t

Li, S., Tang, H., Ge, P., Jiang, F., Zhou, J., Zhang, C., et al. (2018). Electrochemical investigation of natural ore molybdenite (MoS_2) as a first-hand anode for lithium storages. *ACS Appl. Mater. Interfaces* 10, 6378–6389. doi: 10.1021/acsami.7b18571

Li, S., Yang, Y., Xie, M., and Zhang, Q. (2017). Synthesis and electrochemical performances of high-voltage $LiNi_{0.5}Mn_{1.5}O_4$ cathode materials prepared by hydroxide co-precipitation method. *Rare Metals* 36, 277–283. doi: 10.1007/s12598-016-0859-4

Liang, Y., Feng, R., Yang, S., Ma, H., Liang, J., and Chen, J. (2011). Rechargeable Mg batteries with graphene-like MoS_2 cathode and ultrasmall Mg nanoparticle anode. *Adv. Mater.* 23, 640–643. doi: 10.1002/adma.201003560

Liu, G. Y., Lu, Y. P., Zhong, H., Cao, Z. F., and Xu, Z. H. (2012a). A novel approach for preferential flotation recovery of molybdenite from a porphyry copper–molybdenum ore. *Miner. Eng.* 36–38, 37–44. doi: 10.1016/j.mineng.2012.02.008

Liu, H., Su, D., Zhou, R., Sun, B., Wang, G., and Qiao, S. Z. (2012b). Highly ordered mesoporous MoS_2 with expanded spacing of the (002) crystal plane for ultrafast lithium ion storage. *Adv. Energy Mat.* 2, 970–975. doi: 10.1002/aenm.201200087

Liu, K., Feng, J., Kis, A., and Radenovic, A. (2014). Atomically thin molybdenum disulfide nanopores with high sensitivity for DNA translocation. *ACS Nano* 8, 2504–2511. doi: 10.1021/nn406102h

Liu, L., Zhou, W., Peng, Y., Jiao, S., Huang, Y., and Lv, J. (2018). Enhanced lubrication and photocatalytic degradation of liquid paraffin by hollow MoS_2 microspheres. *ACS Omega* 3, 3120–3128. doi: 10.1021/acsomega.7b01587

Liu, W. R., Guo, Z. Z., Young, W. S., Shieh, D. T., Wu, H. C., Yang, M. H., et al. (2005). Effect of electrode structure on performance of Si anode in Li-ion batteries: Si particle size and conductive additive. *J. Power Sources* 140, 139–144. doi: 10.1016/j.jpowsour.2004.07.032

Ma, G., Peng, H., Mu, J., Huang, H., Zhou, X., and Lei, Z. (2013). *In situ* intercalative polymerization of pyrrole in graphene analogue of MoS_2 as advanced electrode material in supercapacitor. *J. Power Sources* 229, 72–78. doi: 10.1016/j.jpowsour.2012.11.088

Roy, T., Tosun, M., Kang, J. S., Sachid, A. B., Desai, S. B., Hettick, M., et al. (2014). Field-effect transistors built from all two-dimensional material components. *ACS Nano* 8, 6259–6264. doi: 10.1021/nn501723y

Shim, J., and Striebel, K. A. (2003). Cycling performance of low-cost lithium ion batteries with natural graphite and $LiFePO_4$. *J. Power Sources* 119–121, 955–958. doi: 10.1016/S0378-7753(03)00297-0

Song, M. K., Cairns, E. J., and Zhang, Y. (2013). Lithium/sulfur batteries with high specific energy: old challenges and new opportunities. *Nanoscale* 5, 2186–2204. doi: 10.1039/c2nr33044j

Stephenson, T., Li, Z., Olsen, B., and Mitlin, D. (2014). Lithium ion battery applications of molybdenum disulfide (MoS_2) nanocomposites. *Energy Environ. Sci.* 7, 209–231. doi: 10.1039/C3EE42591F

Su, S., Zhang, C., Yuwen, L., Liu, X., Wang, L., Fan, C., et al. (2016). Uniform Au@Pt core-shell nanodendrites supported on molybdenum disulfide nanosheets for the methanol oxidation reaction. *Nanoscale* 8, 602–608. doi: 10.1039/C5NR06077J

Sun, D., Ye, D., Liu, P., Tang, Y., Guo, J., Wang, L., et al. (2017). MoS_2/graphene nanosheets from commercial bulky MoS_2 and graphite as anode materials for high rate sodium-ion batteries. *Adv. Energy Mater.* 8:1702383. doi: 10.1002/aenm.201702383

Wagemaker, M., Borghols, W. J. H., and Mulder, F. M. (2007). Large impact of particle size on insertion reactions. A case for anatase $LixTiO_2$. *J. Am. Chem. Soc.* 129, 4323–4327. doi: 10.1021/ja067733p

Wang, J., Wang, Z., Li, X., Guo, H., Wu, X., Zhang, X., et al. (2013b). $xLi_3V_2(PO_4)_3{\cdot}LiVPO_4F$/C composite cathode materials for lithium ion batteries. *Electrochimica Acta* 87, 224–229. doi: 10.1016/j.electacta.2012.09.014

Wang, J.-Z., Lu, L., Lotya, M., Coleman, J. N., Chou, S.-L., Liu, H.-K., et al. (2013a). Development of MoS_2-CNT composite thin film from layered MoS_2 for lithium batteries. *Adv. Energy Mater.* 3, 798–805. doi: 10.1002/aenm.201201000

Wang, L., Zhang, Q., Zhu, J., Duan, X., Xu, Z., Liu, Y., et al. (2018). Nature of extra capacity in MoS_2 electrodes: molybdenum atoms accommodate with lithium. *Energy Storage Mater.* 16, 37–45. doi: 10.1016/j.ensm.2018.04.025

Wang, M., Li, G., Xu, H., Qian, Y., and Yang, J. (2013c). Enhanced lithium storage performances of hierarchical hollow MoS_2 nanoparticles assembled from nanosheets. *ACS Appl. Mater. Interfaces* 5, 1003–1008. doi: 10.1021/am3026954

Wang, P. P., Sun, H., Ji, Y., Li, W., and Wang, X. (2014). Three-dimensional assembly of single-layered MoS_2. *Adv. Mater.* 26, 964–969. doi: 10.1002/adma.201304120

Wang, T., Gao, D., Zhuo, J., Zhu, Z., Papakonstantinou, P., Li, Y., et al. (2013d). Size-dependent enhancement of electrocatalytic oxygen-reduction and hydrogen-evolution performance of MoS_2 particles. *Chemistry* 19, 11939–11948. doi: 10.1002/chem.201301406

Wang, Y., and Ni, Y. (2014). Molybdenum disulfide quantum dots as a photoluminescence sensing platform for 2,4,6-trinitrophenol detection. *Anal. Chem.* 86, 7463–7470. doi: 10.1021/ac5012014

Wu, J., Mu, L., Zhu, J., Feng, X., Lu, X., Larsson, R., et al. (2018). Synthesis of hollow fullerene-like molybdenum disulfide/reduced graphene oxide nanocomposites with excellent lubricating properties. *Carbon* 134, 423–430. doi: 10.1016/j.carbon.2018.04.021

Wu, X., Li, Y., Xiang, Y., Liu, Z., He, Z., Wu, X., et al. (2016). The electrochemical performance of aqueous rechargeable battery of $Zn/Na_{0.44}MnO_2$ based on hybrid electrolyte. *J. Power Sources* 336, 35–39. doi: 10.1016/j.jpowsour.2016.10.053

Wu, X., Xiang, Y., Peng, Q., Wu, X., Li, Y., Tang, F., et al. (2017). Green-low-cost rechargeable aqueous zinc-ion batteries using hollow porous spinel $ZnMn_2O_4$ as the cathode material. *J. Mater. Chem. A* 5, 17990–17997. doi: 10.1039/C7TA00100B

Xiao, J., Choi, D., Cosimbescu, L., Koech, P., Liu, J., and Lemmon, J. P. (2010). Exfoliated MoS_2 nanocomposite as an anode material for lithium ion batteries. *Chem. Mater.* 22, 4522–4524. doi: 10.1021/cm101254j

Xiao, J., Wang, X., Yang, X.-Q., Xun, S., Liu, G., Koech, P. K., et al. (2011). Electrochemically induced high capacity displacement reaction of PEO/MoS_2/graphene nanocomposites with lithium. *Adv. Funct. Mater.* 21, 2840–2846. doi: 10.1002/adfm.201002752

Xiao, J.K., Zhang, W., Liu, L. M., Zhang, L., and Zhang, C. (2017). Tribological behavior of copper-molybdenum disulfide composites. *Wear* 384–385, 61–71. doi: 10.1016/j.wear.2017.05.006

Xie, X., Ao, Z., Su, D., Zhang, J., and Wang, G. (2015). MoS_2/graphene composite anodes with enhanced performance for sodium-ion batteries: the role of the two-dimensional heterointerface. *Adv. Funct. Mater.* 25, 1393–1403. doi: 10.1002/adfm.201404078

Yang, E., Ji, H., and Jung, Y. (2015). Two-dimensional transition metal dichalcogenide monolayers as promising sodium ion battery anodes. *J. Phys. Chem. C* 119, 26374–26380. doi: 10.1021/acs.jpcc.5b09935

Yang, T., Chen, Y., Qu, B., Mei, L., Lei, D., Zhang, H., et al. (2014). Construction of 3D flower-like MoS_2 spheres with nanosheets as anode materials for high-performance lithium ion batteries. *Electrochimica Acta* 115, 165–169. doi: 10.1016/j.electacta.2013.10.098

Yang, Y., Huang, G., Xie, M., Xu, S., and He, Y. (2016). Synthesis and performance of spherical $LiNixCoyMn_1$-x-yO2 regenerated from nickel and cobalt scraps. *Hydrometallurgy* 165, 358–369. doi: 10.1016/j.hydromet.2015.11.015

Yang, Y., Huang, G. Y., Sun, H., Ahmad, M., Mou, Q., and Zhang, H. (2018). Preparation and electrochemical properties of mesoporous $NiCo_2O_4$ double-hemisphere used as anode for lithium-ion battery. *J. Colloid Interface Sci.* 529, 357–365. doi: 10.1016/j.jcis.2018.06.039

Yang, Y., Li, S., Zhang, Q., Zhang, Y., and Xu, S. (2017). Spherical agglomeration of octahedral $LiNi_{0.5}Co_4xMn_{1.5-3}xO_4$ cathode material prepared by a continuous coprecipitation method for 5 V lithium-ion batteries. *Ind. Eng. Chem. Res.* 56, 175–182. doi: 10.1021/acs.iecr.6b03657

Yoshio, M., Wang, H., and Fukuda, K. (2003). Spherical carbon-coated natural graphite as a lithium-ion battery-anode material. *Angew. Chem.* 115, 4335–4338. doi: 10.1002/ange.200351203

Yoshio, M., Wang, H., Fukuda, K., Umeno, T., Abe, T., and Ogumi, Z. (2004). Improvement of natural graphite as a lithium-ion battery anode material, from raw flake to carbon-coated sphere. *J. Mater. Chem.* 14, 1754–1758. doi: 10.1039/b316702j

Zhang, Q., Chen, H., Luo, L., Zhao, B., Luo, H., Han, X., et al. (2018). Harnessing the concurrent reaction dynamics in active Si and Ge to achieve high performance lithium-ion batteries. *Energy Environ. Sci.* 11, 669–681. doi: 10.1039/C8EE00239H

Zhang, Q., Wang, J., Dong, J., Ding, F., Li, X., Zhang, B., et al. (2015). Facile general strategy toward hierarchical mesoporous transition metal oxides arrays on three-dimensional macroporous foam with superior lithium storage properties. *Nano Energy* 13, 77–91. doi: 10.1016/j.nanoen.2015.01.029

Zhang, X., Lai, Z., Tan, C., and Zhang, H. (2016). Solution-processed two-dimensional MoS_2 nanosheets: preparation, hybridization, and applications. *Angew. Chem.* 55, 8816–8838. doi: 10.1002/anie.201509933

Zheng, Z., Zao, Y., Zhang, Q., Cheng, Y., Chen, H., Zhang, K., et al. (2018). Robust erythrocyte-like Fe_2O_3@carbon with yolk-shell structures as high-performance anode for lithium ion batteries. *Biochem. Eng. J.* 347, 563–573. doi: 10.1016/j.cej.2018.04.119

Zhu, C. B., Mu, X. K., van Aken, P. A., Yu, Y., and Maier, J. (2014). Single-layered ultrasmall nanoplates of MoS_2 embedded in carbon nanofibers with excellent electrochemical performance for lithium and sodium storage. *Angew. Chem.* 53, 2152–2156. doi: 10.1002/anie.201308354

Zhu, H., Zhang, J., Yanzhang, R., Du, M., Wang, Q., Gao, G., et al. (2015). When cubic cobalt sulfide meets layered molybdenum disulfide: a core-shell system toward synergetic electrocatalytic water splitting. *Adv. Mater.* 27, 4752–4759. doi: 10.1002/adma.201501969

Conflict of Interest Statement: The authors declare that the research was conducted in the absence of any commercial or financial relationships that could be construed as a potential conflict of interest.